Myelin membrane wrapping of CNS axons by PI(3,4,5)P3-dependent polarized growth at the inner tongue

Nicolas Snaidero[1,2], **Wiebke Möbius**[3,9], **Tim Czopka**[4], **Liesbeth H.P. Hekking**[5], **Cliff Mathisen**[5], **Dick Verkleij**[5], **Sandra Goebbels**[3], **Julia Edgar**[3], **Doron Merkler**[6,7,8], **David A. Lyons**[4], **Klaus-Armin Nave**[3], and **Mikael Simons**[1,2,*]

[1]Max Planck Institute of Experimental Medicine, Cellular Neuroscience, Hermann-Rein-Strasse. 3, 37075, Göttingen, Germany [2]Department of Neurology, University of Göttingen, Robert-Koch-Strasse. 40, 37075, Göttingen, Germany [3]Department of Neurogenetics, Max Planck Institute of Experimental Medicine, Hermann-Rein-Strasse. 3, 37075, Göttingen, Germany [4]Centre for Neuroregeneration, University of Edinburgh, Edinburgh EH16 4SB, UK [5]FEI Company, Achtseweg Noord 5, 5651 GG Eindhoven, The Netherlands [6]Department of Pathology and Immunology, University of Geneva, 1211 Geneve, Switzerland [7]Division of Clinical Pathology, Geneva University Hospital, 1211 Geneve, Switzerland [8]Department of Neuropathology, University of Göttingen, 37075 Göttingen, Germany [9]Center for Nanoscale Microscopy and Molecular Physiology of the Brain (CNMPB), 37075 Göttingen, Germany

Summary

Central nervous system myelin is a multilayered membrane sheath generated by oligodendrocytes for rapid impulse propagation. However, the underlying mechanisms of myelin wrapping have remained unclear. Using an integrative approach of live imaging, electron microscopy and genetics, we show that new myelin membranes are incorporated adjacent to the axon at the innermost tongue. Simultaneously, newly formed layers extend laterally ultimately leading to the formation of a set of closely apposed paranodal loops. An elaborated system of cytoplasmic channels within the growing myelin sheath enables membrane trafficking to the leading edge. Most of these channels are closing with ongoing development, but can be re-opened in adult by experimentally raising phosphatidylinositol-(3,4,5)-triphosphate levels, which reinitiates myelin growth. Our model can explain assembly of myelin as a multilayered structure, abnormal myelin outfoldings in neurological disease, and plasticity of myelin biogenesis observed in adult life.

Introduction

In the vertebrate nervous system, axons are ensheathed with myelin, which is one of the most remarkable and complex transformations of a plasma membrane (Jessen and Mirsky, 2005; Sherman and Brophy, 2005; Salzer et al., 2008). More than 60 years after the seminal discovery demonstrating that myelin is made by axon-associated glial cells and not by the axon itself (Ben Geren, 1954), the molecular mechanisms by which the myelin sheath is

*Correspondence to: M. Simons, Max Planck Institute of Experimental Medicine, Hermann-Rein-Strasse. 3, 37075, Göttingen, Germany; phone: +49-551-3899533; fax: +49-551-3899201; msimons@gwdg.de.

wrapped around the axon are still largely unknown. This is due in part to the physical limitations of visualizing membrane dynamics at the nanometer scale and the time span involved (i.e. days in vivo). Even if it represents "textbook knowledge" that oligodendrocytes wrap myelin around an axon by steering a leading process that stays in close contact with the axon, we have almost no experimental data to substantiate this claim. Does the leading edge resemble a glial growth cone-like extension related to the one that drives axonal outgrowth in developing neurons? It has also become apparent that myelin is a dynamically active structure (Young et al., 2013) that can provide metabolic support to associated axons (Funfschilling et al., 2012; Lee et al., 2012). However, it remains completely unclear how molecules reach the innermost myelin layer, i.e. passing through a multilamellar stack of membranes.

A number of different models have been proposed to explain how a myelin sheath might form in development. According to the "carpet crawler" model (Bunge et al., 1961; Bunge et al., 1989), the oligodendrocyte forms a process that broadens and extends along the entire axonal segment (the future internode) before it makes one turn and moves underneath the growing sheet. However, at least in the CNS, several morphological features of myelin are incompatible with this model. In particular, it is clear from electron microscopic analysis that the number of myelin layers can vary along the length of a single myelin sheath during its formation (Knobler et al., 1976). Moreover, the molecular forces necessary to continuously displace myelin by newly made layers of membrane from underneath might be too high. Some of these shortcomings were reconciled in the "liquid croissant" (Sobottka et al. 2011) and the "yo-yo" model (David Colman, personal communication). In the latter case, myelin growth begins with a single glial process that, after making axonal contact, spirally encircles the future internode, followed by the lateral growth of the individual membrane layers. However, due to the physical limitations of imaging such processes it has not been possible to experimentally support any of these models of myelin wrapping.

Here, by combining an array of techniques (in vivo live-imaging, serial block-face imaging by focused ion beam, high pressure freezing and a virus as a reporter) we show that myelin growth occurs by the consecutive wrapping of the inner tongue (leading edge) around the axon and the coordinated lateral extension of the individual layers of myelin. Cytoplasmic sub-domains at the end of each myelin layer remain in close contact with the underlying axon moving laterally and around the axon towards the future node where they eventually form a set of closely apposed "paranodal loops." Together our data elucidate mechanisms of myelin sheath morphogenesis and its regulation throughout life.

Results

Visualisation of nascent myelin sheath morphogenesis *in vivo*

In order to visualise the dynamics of myelin sheath formation *in vivo* we included the zebrafish as a model organism, given its amenability for high-resolution *in vivo* imaging (Kirby et al., 2006). In order to resolve the initial wrapping events of CNS myelination we utilized the Tg(nkx2.2a:meGFP) line, which expresses a membrane tethered GFP in early myelinating oligodendrocytes (Kirby et al., 2006; Czopka et al., 2013). We imaged these early myelination events and plotted the fluorescence intensity profiles along the length of

32 short (less than 10μm in length) nascent myelin sheaths and found that fluorescence intensity was consistently higher in the central regions of the sheaths relative to their ends (Figure 1A-C; S1). By electron microscopy we found that most of the myelin sheaths with less than 4 wraps were still in an uncompacted state (Figure S1). We hypothesised that the change in fluorescence intensity might reflect differences in the number of wraps of myelin membrane around the axon at different points along the myelin sheath. In order to address this possibility we performed quantitative fluorescence intensity analyses of deconvolved confocal images taken through single myelin sheaths. This analysis revealed that the changes in fluorescence intensity along the length of a myelin sheath did indeed occur in quantal steps, suggesting differences in the number of wraps of myelin membrane along the axon, rather than random fluctuations of fluorescence signal intensity (Figure S1). When measuring how fluorescence intensities moved over time, we observed that along the axon not only the edges of the myelin segments extended laterally but also the step-like fluorescence patterns (Figure 1A,B, S1). Such dynamic changes in fluorescence intensity were only observed during the first few hours following initiation of myelin sheath formation. At later stages of myelin sheath maturation with a sheath length of more than 10 μm (observed using Tg(mbp:EGFP-CAAX)) the fluorescence intensity profiles along the length of individual sheaths were more complex, presumably due to an increased number of wraps and the exclusion of membrane tethered GFP from the compact myelin sheaths (Figure 1D,E). Quantification of 25 mature and longer myelin sheaths showed that fluorescence intensity was on average uniform along the length of such mature sheaths (Figure 1F).

Thus, myelin growth appears to start non-uniformly at the centre of nascent myelin sheaths and continues by lateral extension of developing layers towards the future nodes, which is consistent with a previous model of myelin growth (Sobottka et al. 2011).

Three-dimensional reconstruction of growing myelin sheaths

Since time-lapse imaging with light microscopy is not able to resolve single myelin layers, we used electron microscopy to investigate their spatial organization during myelination in mice. We first analyzed mouse optic nerves at postnatal day (P) 10, when myelin could be captured at all stages of growth with a minimal amount of mature sheaths. For sample preparation we used high pressure freezing (HPF) followed by freeze substitution on fresh optic nerve to avoid artifacts typically introduced by chemical fixation.

To understand the spatial organization of a growing myelin sheath we performed serial block-face imaging by focused ion beam milling in the SEM (FIB-SEM) to obtain high-resolution three-dimensional reconstructions of the optic nerve at P10 (Figure 2A-C). The imaged volumes comprised 16μmx14μmx40-55μm(X, Y, Z) with a lateral resolution of 4-6nm and a Z-resolution of 50nm.

Within these volumes we identified and reconstructed the cytoplasm-rich areas of the developing myelin sheath of 45 individual axons from three different animals to analyze the pattern of myelin growth. A representative three-dimensional reconstruction of such myelinated fibers is shown in Figure 2 and Movie S3 illustrates the typical features of a growing myelin sheath. We found that the thickest part of myelin is found where the process

of the oligodendrocyte is connected to the myelin sheath. In addition, we observed that the outermost membrane layer spans the entire myelin segment length with only minimal winding around the developing sheath (depicted in purple in Figure 2A,B,F). In contrast, the three-dimensional reconstructions of the inner tongue clearly illustrate that it winds much more frequently around the axon as compared to the outer tongue. The average lateral distance between 2 successive windings is ~6μm along the entire myelin segment - extending from the lateral edge with the thinnest (2 wraps: Figure 2D) up to the oligodendrocytic process where the myelin was the thickest (11 wraps: Figure 2E). A mirror pattern could be observed towards the other end of the sheath (Figure 2C,F). We could confirm these morphological features using ultrathin longitudinal sections of P10 optic nerve prepared for transmission electron microscopy (TEM) where individual membrane layers of myelin were discernible over an average distance of 20μm (60 myelination events from three different animals) (Figure 2G). On longitudinal sections of the myelin sheath the lateral endings of each individual layers appear as a cytoplasmic-rich edge. The distance between these lateral cytoplasmic-rich edges of the successive layers along the length of the myelin sheath was ~5.2μm in average (Figure 2G, S2). When we quantified the number of myelin layers relative to their distance from the oligodendrocyte process, we found that it was highest at the position where the oligodendrocyte process feeds into the myelin sheath and became lower with increasing distance at both edges of the growing myelin sheath (Figure 2C,G; Movie S4).

Next, we compared these early myelination profiles with later stages of development. When myelin structure was investigated on longitudinal sections at P23 and P60 (60 myelination profiles from three different animals), the distance of the lateral cytoplasmic-rich edges of the successive layers along the length of the myelin sheath increased from around 5.2μm at P10, to ~34.2μm at P23 and to ~ 137.3μm at P60 (Figure S2). Correspondingly, when the formation of the paranodes during the maturation of the myelin sheath was assessed, the distance between successive cytoplasmic-rich edges of the layers was continuously declining with time until the paranodal loops were fully established at P60 (from ~2.5μm at P10 to ~0,3μm at P23 and ~0.2μm at P60) (Figure S2).

Based on the shape of the myelin layers and their development over time our model suggests that a growing myelin sheath winds around the axon by an advancing inner tongue (underneath the previously deposited membrane) in the center of the myelin segment. Concurrent to this radial growth of the sheath the layers extend laterally towards the node of Ranvier. This corresponds to our observations in live animals that membrane fluorescence intensity is at first higher at the centre of a myelin sheath than at the lateral edges and evens with time.

Polarized transport of the vesicular stomatitis virus G protein to the inner tongue

EM reconstructions provide static images with high resolution and time-lapse imaging using light microscopy is not able to visualize adjacent myelin layers. We therefore sought of other methods to resolve at subcellular resolution where newly synthesized membrane components are incorporated into the growing myelin sheath. To visualize the site where proteins are integrated into the myelin sheath, a large amount of a membrane-associated

reporter protein needs to be generated in a short time to allow its detection before the protein diffuses away into the growing sheath. Therefore we used the vesicular stomatitis virus (VSV) to express glycoprotein G (VSV-G) as a tool, a well-established reporter of membrane protein trafficking within the biosynthetic pathway (Farquhar, 1985). To directly analyze the trafficking, first cultured oligodendrocytes were infected with VSV and analyzed at 2, 3 and 4 hours post-infection. At 2 hours post-infection VSV-G accumulated within the cell body and the cytoplasmic channels of the sheet in the Golgi-complex and in vesicular structures, but did not yet reach the membrane surface (Figure S3). Starting at 3 hours post-infection VSV-G was detectable at the cell surface and, interestingly, showed enrichment at the F-actin rich rim of the cell (Figure S3). The enrichment at the rim was not due to a larger membrane area e.g. membrane folds, because the comparison to cells at 4 hours post-infection revealed that this enrichment diminished over time (Figure S3). Therefore, we conclude that insertion of VSV-G did not occur randomly in the cell, but selectively in the most distal region from where the proteins can diffuse backwards into the sheets.

We next investigated whether we could also use this system *in vivo* by localizing VSV-G or virus budding sites in myelinating oligodendrocytes. High-titer stocks of VSV were injected into the corpus callosum of P21 and P60 mice that were sacrificed 3 and 6 hours later. Immunoelectron microscopy at 3 and 6 hours post-infection showed that large amounts of VSV-G preferentially accumulated in the inner tongue membrane of the myelin sheath and much less in the outer tongue (Figure 3A,E,S3). The antibody used was of high specificity as no background staining could be observed in control-injected animals (Figure 3D). At 6 hours post-infection this preferential distribution of the VSV-G at the inner tongue had increased even further (Figure S3). In addition, after 6 hours of infection, we observed an accumulation of viral particles at the inner tongue of the growing myelin sheath (Figure S3). In contrast, when VSV was injected into the corpus callosum of mice at P60 when myelin biogenesis is terminated, most of the labelling was found in the outer tongue and there was hardly any VSV-G labelling at the inner tongue at 6 hours post-infection (Figure 3B,C).

Our results suggest that membrane trafficking in myelinating oligodendrocytes is polarized as new membrane protein is targeted and selectively inserted at the inner tongue of the growing myelin sheath.

Cytoplasmic channels provide direct connections to the leading edge

A myelin growth zone at the inner tongue would require transport of newly synthesized membrane components from the soma though the oligodendroglial process. In principle, vesicles could traffic through cytoplasmic channels from the outside to the inside of the sheath along the helical coil that we have defined. In the PNS an additional connection of the outer and inner tongues of myelin is provided by the Schmidt-Lanterman incisures, but these structures have rarely been observed in CNS myelin (Blakemore, 1969; Hildebrand et al., 1993). However, in this study we used high pressure freezing and freeze-substitution to better preserve the native myelin structure for electron microscopy in order to analyze how prevalent cytoplasmic channels really are. Surprisingly, using this method, at the peak of myelination (P10) we observed a large number of myelin sheaths with cytoplasmic channels providing a short connection from the outer and inner tongue of myelin (Figure 4A-C).

There was a gradual reduction of these cytoplasmic channels with the further development of the myelin sheaths (Figure 4C). At P60 they had almost completely disappeared (Figure 4C). At P10 vesicular structures were frequently observed within the cytoplasmic channels, as well as in the inner and outer tongue covering ~12% of the cytoplasmic area (Figure S4). Later in development, concomitant with the disappearance of the cytoplasmic channels there was a dramatic decrease in the cytoplasmic area covered by vesicles (Figure S4). The three dimensional reconstruction of a representative myelination profile at P10 shows a cytoplasmic channel system (Figure 4D in red) that runs through a compact myelin sheath and ends at two points in the inner tongue (Figure 4E,F).

Furthermore, the three dimensional reconstructions based on the serial block face imaging data set show that some cytoplasmic channels appear to run into and end within myelin outfoldings (Figure 4E,G). Myelin outfoldings (Figure 4G,H), also termed 'redundant myelin', have previously been considered pathological features associated with different myelin diseases including dysmyelinating neuropathies (Pereira et al. 2012). Here, we find that 6.5% of the myelinated axons had outfoldings in cross-section analysis of P10 optic nerve (Figure 4I). Based on the three-dimensional reconstruction with serial block face imaging, we determined that outfoldings have a width of around 10μm; and since a myelin sheath has an average length of around 100μm, we then estimated that at least half of the myelinated segments should have outfoldings at P10 in the optic nerve. Interestingly, myelin outfoldings almost completely disappeared at P60 (Figure 4I). The disappearance of the myelin outfodings correlated with the formation of the radial component by Claudin-11, a tight-junction component that fixes the adjacent layers of myelin membrane (Figure S4).

Together, these observations support the idea that the cytoplasmic channels are involved in facilitating the efficient delivery of membrane material to the active growth zone of the inner layers, which in some cases leads to transient focal hypermyelination as seen by the generation of myelin outfoldings (Figure S4).

Regulation of myelin growth by PI(3,4,5)P3 *in vivo*

Taken together, our data suggest that newly synthesized myelin membrane is directed through a system of cytoplasmic channels towards the inner tongue before fusing with the growing myelin sheath. If this is true, we should be able to affect the size and abundance of cytoplasmic channels by stimulating myelin growth. Indeed, the growth of the myelin sheath *in vivo* was associated with a larger inner, but not outer tongue, when compared to later stages of development (Figure 5A,B). A key pathway that regulates myelin growth is the PI3K/AKT/mTOR signaling pathway (Flores et al., 2008; Tyler et al., 2009; Goebbels et al., 2010).

Thus, we analyzed whether PI(3,4,5)P3 elevation i*n vivo* would influence the frequency of cytoplasmic channels and the size of the inner tongue and in so doing promote myelin growth. Indeed, when myelin was analyzed in the optic nerves after conditional inactivation of *Pten*, which leads to PI(3,4,5)P3 elevation at P23 and P60 a much larger inner tongue and more cytoplasmic channels were observed as compared to the control whereas the size of the outer tongue was unaffected (Figure 5C-D,H-J). In addition, when we investigated myelin structure on longitudinal sections at P23 and P60, we found that in contrast to wild-type

animals where the cytoplasmic-rich edges had assembled into paranodes, a large number of cytoplasmic-rich edges were still found along the length of the myelin sheath in *Pten* deficient mice (Figure 5E,F). Furthermore, the area covered by vesicular profiles within the uncompacted areas of the myelin sheath was much higher in the *Pten* deficient mice as compared to wild-type at P23 and P60 (Figure 5G). Thus, all of the key morphological features observed in the developing myelin sheaths of wild-type animals that are lost in mature adult sheaths reappear in the adult hypermyelinating *Pten* mutants confirming a role of these features in myelin growth.

We also asked whether re-initiation of myelin growth involves the re-opening of these channels after completion of developmental myelination. To test this we analyzed *Pten$^{flox/flox}$*Plp1-CreERT2* mice 4 weeks after tamoxifen-induced conditional inactivation of *Pten* in oligodendrocytes at P100. We found in the optic nerve that a large number of channels re-appeared (Figure 5K,L), at a time when the number of myelin wraps was unaltered (Figure 5M). To determine whether the opening of the channels was followed by an increase in myelin wrapping, we analyzed *Pten$^{flox/flox}$*Plp1-CreERT2* mice 12 weeks after tamoxifen injection. Indeed, we did observe that, in addition to an increase of cytoplasmic channels, myelin was significantly thicker, suggesting that re-opening of the cytoplasmic channels precedes renewed myelin growth (Figure 5N,O). Thus, the cytoplasmic channels appear to be dynamic and have the potential to re-open after the developmental program is terminated.

Regulation of membrane trafficking by PI(3,4,5)P3 to the leading edge *in vitro*

We next asked whether PI(3,4,5)P3 regulates membrane trafficking in oligodendrocytes. To this end, we turned to cell culture experiments and firstly confirmed that the size of the cellular rim of cultured oligodendrocytes increased during cellular growth and was enriched in F-actin, PI(3,4,5)P3 and Phospho-Akt (Figure S5). In order to verify that the outer rim of an oligodendrocyte in culture corresponds to the inner tongue of myelin *in vivo,* we analyzed whether there was a similar enrichment of F-actin in the inner tongue of the myelin sheath in the mouse during the active phase of myelination. Indeed, F-actin colocalized in a patch-like structure with MAG, which resides at the adaxonal membrane, but to a lesser extent with MBP, a marker of compact myelin (Figure S5) as described in the PNS (Trapp et al., 1989). In contrast, at P60 when the active growth phase of myelin has passed, F-actin was undetectable (Figure S5). Next, we determined whether the size of the outer rim/leading edge is influenced by the PI(3,4,5)P3/Akt signaling pathway. By applying a panel of well-characterized inhibitors or activators we found that inhibition of PI(3,4,5)P3/Akt signalling resulted in thinning of the leading edge, whereas the activation using a PTEN inhibitor had the opposite effect (Figure S5). We then asked whether PI(3,4,5)P3 directly guides membrane trafficking in oligodendrocytes and applied a method to artificially polarize cell growth. Electrical signals are known to regulate cell migration by the activation of PTEN dependent signaling and polarized elevation of PI(3,4,5)P3 (Zhao et al., 2006). When oligodendrocytes were cultured in an electrical field using physiologically relevant currents (1Volt/cm^2 for 2.5hours) we observed that Phospho-Akt distribution was found polarized towards the cathode in 70% of the cells (Figure S5). When cell were infected with VSV and membrane trafficking was followed 3 hours post-infection, the targeting of VSV-G occurred

preferentially towards the cathode (Figure S5). Thus, our results demonstrate that in cultured oligodendrocytes membrane trafficking of VSV-G is not random, but polarized towards a growing edge in cultured oligodendrocytes.

Regulation of myelin membrane compaction by MBP and CNP

In addition to the membrane transport along the biosynthetic pathway, cytoplasmic components also need to be delivered to myelin. MBP is the major cytoplasmic component of myelin and is known to mediate the compaction of the cytoplasmic leaflets of the myelin lamellae, a process that excludes most cytoplasm from the developing myelin sheath and which is necessary to provide myelin with the crucial physical stability for myelin membrane wrapping (Figure S6). As previously shown in multiple electron microscopy analysis of myelin (Hildebrand et al., 1993) compaction is fast and starts early in development after a few wraps. To analyze the process of myelin compaction in more detail we investigated the extent of compaction at the age of 10, 14 and 21 days in the optic nerves of wild-type and heterozygote *shiverer* mice in which myelin compaction is expected to occur slower due to decreased MBP expression levels. In wild-type nerves studied at P10, 12% of myelinated axons, were not yet fully "compacted" (Figure 6A,B). Our high-resolution EM analyses showed that compaction almost invariably appears first in the outermost layers of myelin (Figure S6) suggesting that the addition of new layers by the growth of the inner tongue occurs faster than the MBP-mediated compaction. Importantly, in optic nerves of heterozygote *shiverer* mice, more myelin sheaths with uncompacted wraps were detected. In addition, the number of compacted membrane layers in relation to the total number of myelin layers was lower compared to wildtype at P10 and P14 (Figure S6). At the age of P21 no significant differences were detectable between these genotypes (Figure 6B).

MBP mRNA is transported to the growing tip of oligodendroglial processes (Ainger et al., 1993) and translation of MBP is induced at the innermost myelin layers that are in contact with the axon (Colman et al., 1982; Trapp et al., 1987; Wake et al., 2011; Laursen et al., 2011). However, when we analysed the subcellular distribution of MBP protein in the myelin sheath by immunoelectron microscopy the levels of MBP were four-fold lower in the inner uncompacted wraps as compared to the outer compacted layers (Figure 6C,D). Thus, we hypothesized that there must be active mechanisms that prevent myelin compaction at the innermost regions of myelin. Since these non-compacted wraps were enriched in CNP (Figure S6), we analyzed its role in this process. Indeed, when the optic nerves of heterozygote and homozygotes CNP deficient mice were examined by high pressure freezing EM at P10, a dramatic reduction of the uncompacted myelin wraps were observed. Whereas ~ 12% of myelin sheaths contained uncompacted wraps in wild-type mice, there was a reduction to ~ 4% in CNP +/- and to less than 1% in CNP -/- mice (Figure 6E). Thus, our results show that the equilibrium of CNP and MBP levels appears to regulate the speed of compaction in early development. Hence, we conclude that the rapid extension of the inner most tongue during myelin growth together with the accumulation of CNP between these newly synthesized layers prevent the premature compaction of myelin by MBP at the leading edge.

Discussion

The aim of this study was to answer a fundamental question of axon-glia interactions in the vertebrate nervous system: how does an oligodendrocyte "wrap" its plasma membrane around the axon? In this study we have combined data from very different experimental approaches that have led us to a novel model of myelin membrane growth in the central nervous system, which is summarized in Figure 7, S7 and in Movie S5: we suggest that myelin grows by two coordinated motions – the wrapping of the leading edge at the inner tongue in a triangle-like shape around the axon underneath the previously deposited membrane, together with the lateral extension of myelin membrane layers towards the nodal regions. In this model, the lateral cytoplasmic domains of each myelin layer are always in contact with the axonal surface and move in a continuous helical manner towards the future node where they align and form the paranodal loops. An elaborated system of cytoplasmic channels within compacted myelin provides short-cuts for the transport of membrane to the growth zone at the inner tongue in the developing myelin sheath. Most channels appear transiently in development at the most intense phase of membrane growth and are regulated by PI(3,4,5)P3 levels.

We used electron microscopy of high pressure frozen samples and three dimensional reconstruction based on serial block face to obtain snap shots of myelin ultrastructure during development of the optic nerve. We find that the innermost layer of myelin has the shortest lateral extension whereas the layers towards the top of the myelin sheath build up in size with each consecutive wrap. Previous studies using light microscopy have observed a coil of an average periodicity of 5.7 to 7μm along the internodal dimension (Pedraza et al., 2009; Sobottka et al., 2011; Ioannidou et al., 2012). This has led to the suggestion that myelin extends as a coil twisting across the axon in a corkscrew motion (Pedraza et al., 2009) or that myelin thickening is achieved by forming new layers on to top of the inner ones in a "croissant-like" manner (Sobottka et al., 2011). One limitation of these studies is that they are almost entirely based on light microscopy. However, in our three dimensional EM reconstructions we do not detect a serpent-like process coiling around the axon nor a "croissant-like" structure. A possible explanation for the conclusions of the previous studies could be the time point when myelination was analyzed. In the very initial stage, the myelin layers may indeed show overlapping profiles at the surface of the forming sheath. However, we find that during myelin growth the outermost myelin layer is continuous along the entire length of the sheath. The pattern of the coiling helix arises from the organization of the inner layers of myelin within the myelin sheath along the axon. In addition, and as has been noted previously (Webster, 1971; Knobler et al., 1976), the non-uniform thickness of the growing myelin internode is also incompatible with a "carpet crawler" type of model where myelin grows uniformly around the axon. A major limitation of all of the previously proposed models is that the leading edge was not defined. By using a virus as a reporter, we were able to follow membrane trafficking within the forming myelin sheath and define the inner tongue as the growth zone.

In addition, to membrane transport via the biosynthetic secretory pathway, cytoplasmic components need to be delivered to myelin. MBP is the major cytoplasmic component and its mRNA is transported in cytoplasmic granules to myelin, where the local translation of

MBP is initiated and the compaction of the cytoplasmic surfaces triggered (Colman et al., 1982). We observed that the targeting and the deposition of myelin membrane components are spatially separated in the growing myelin sheath. Whereas vesicular transport is directed towards the inner tongue of the myelin sheath, MBP-mediated compaction occurs first in the outer layers and moves inward with time. We propose that even if MBP is synthesized in the front, compaction is not fast enough to keep up with the rapid extension of the inner most tongue during myelin growth. In addition, we identified CNP, a protein previously implicated in maintaining axonal integrity (Lappe-Siefke et al., 2003), as a factor that delays myelin compaction. In the absence of CNP, myelin compaction appeared to proceed faster and extend to the inmost layers of the myelin sheath. These data are consistent with previous work in a transgenic mouse line showing that overexpression of CNP result in areas that lack myelin compaction (Gravel et al., 1996). Taken together, we hypothesize that MBP is synthesized in the distal (close to the axon) areas of myelin followed by its diffusion backwards to the outermost area where compaction is initiated. Once MBP is bound to the two adjacent cytoplasmic surfaces it polymerizes into fibrous network thereby greatly reducing its mobility and establishing a nucleation point for myelin membrane zippering (Aggarwal et al., 2013). This fusion of the adjacent cytoplasmic surfaces of the myelin bilayer is necessary to provide myelin with the crucial physical stability for myelin membrane wrapping. We hypothesize that myelin wrapping is maintained by tightly regulating growth and compaction together to ensure that a stable (Toyama et al., 2013) and tightly condensed membrane is driven multiple times around the axon.

Another important question is how membrane trafficking is polarized towards the leading edge. PI3-kinase activation and its lipid product PI(3,4,5)P3 are known to play instructive roles in cell polarization by recruiting and activating the small RhoGTPases at the leading edge (Ridley, 2011). Axonal signal may also regulate myelin growth. Electrical activity, for example, influence myelination in the CNS possibly by effectors such as neurotransmitters, ATP, ions or growth factors (Barres and Raff, 1993; Demerens et al., 1996; Fields and Stevens-Graham, 2002). We found that an electrical field was sufficient to polarize the leading edge and membrane trafficking towards the cathode. Such electrical fields might be generated by the local accumulation of K^+ when released from spiking axons.

Another way to guide membrane trafficking to the leading edge is provided by the cytoplasmic channels with the myelin sheath. The detection of numerous cytoplasmic channels in developing myelin was unexpected as Schmidt-Lantermann incisures-like structures were not thought to be abundant in CNS myelin (Bunge, 1968). An important technical advancement that made the visualization of cytoplasmic channels possible was high-pressure freezing of fresh tissue for electron microscopy, which results in preservation of tissue architecture close to native state. Injection of fluorescent dyes into freshly isolated spinal cord slices has also revealed an extensive network of interconnected cytoplasmic pockets in myelin (Velumian et al., 2011).

Recent studies suggest that activity dependent myelination should not only be considered in development (Wake et al., 2011), but also in nervous system plasticity in postnatal development and adulthood (Liu et al., 2012; Makinodan et al., 2012; Young et al., 2013). Notably, social isolation reportedly impairs myelination in the prefrontal cortex in young

mice, whereas social re-integration is sufficient to normalize myelin formation (Liu et al., 2012). Consistent with the concept of adult myelin plasticity, myelin growth can be experimentally reactivated even if the developmental program has been terminated (Goebbels et al., 2010). Here we show that the cytoplasmic channels re-open when PI(3,4,5)P3 levels are increased in the adult mice, which was followed by an increase in myelin thickness. Thus, this elaborated network of interconnected tunnels is dynamic and provides a mean to transport molecules through the internode even in fully developed myelin sheaths. One interesting question is how the formation of the cytoplasmic channels is regulated. An attractive hypothesis is that PI(3,4,5)P3 induces local actin polymerization at the cytoplasmic leaflet of the myelin bilayer, which covers and protects myelin from being compacted by MBP. It is possible that there is a tug-of-war type of regulation of the cytoplasmic channels by PI(3,4,5)P3 effectors such as the actin cytoskeleton possibly in association with CNP holding MBP back from membrane compaction.

We show that some cytoplasmic channels end within the myelin outfoldings and we therefore propose that myelin outfoldings form by the preferential delivery of membrane through cytoplasmic channels into the inner tongue resulting in focal accumulation of excess membrane that extends outwards. These myelin outfoldings have previously been considered pathological features associated with different myelin diseases including dysmyelinating neuropathies. However, here we clearly show that myelin outfoldings are part of the normal development of myelin in the optic nerve. When cytoplasmic channels close these outfoldings may slowly spread out due to the fluidity of the membrane. Thus, outfoldings may serve as membrane reservoirs to allow the completion of the lateral growth of the layers and secure unperturbed radial growth of the myelinated axon itself, which would explain their gradual disappearance later in life.

Taken together, we have used an in-depth integrated approach of advanced imaging at the light and electron microscopic level to dissect the morphogenesis of myelin membrane wrapping. Combined with the discovery of the previously unknown growth zone of myelin and of transient cytoplasmic channels in myelin that allow membrane trafficking towards the growing tip, our observations lead to a novel model of myelin wrapping. This model not only fills a gap in our understanding of myelin biogenesis in brain development, but also sheds new light on myelin pathology in various neurological diseases in which myelination is perturbed.

Experimental Procedures

Full details are provided in the Extended Experimental Procedures

Fish husbandry

The transgenic zebrafish lines Tg(nkx2.2a:mEGFP) and Tg(mbp:EGFP-CAAX) were used in this study. The imaging is described in the Extended Experimental Procedures.

Mice and primary cell culture

The generation of PTEN cre/+ flox/floxPten and CNP mutant mice has been described previously (Goebbels et al., 2010; Lappe-Siefke et al., 2003). The *shiverer* mice lacking

MBP were maintained on a C57Bl6 background. The primary oligodendrocyte cell culture was prepared as described previously (Aggarwal et al., 2013).

Electron microscopy

Mice were killed by cervical dislocation and freshly extracted optic nerves were cryo-fixed using a high pressure freezer HPM100 (Leica, Vienna, Austria) and further processed by freeze substitution and EPON-embedding following the "tannic acid-OsO$_4$ protocol" described in (Mobius et al., 2010). Cross and longitudinal ultrathin sections were obtained with a Ultracut S ultramicrotome (Leica, Vienna, Austria) and contrasted as described (Mobius et al., 2010). Sections were imaged using a LEO 912 Omega electron microscope (Zeiss, Oberkochen, Germany) equipped with an on-axis 2k CCD camera (TRS, Moorenweis, Germany). Three to five animals were used for each analysis. On cross sections five to ten randomly selected areas of 150 μm^2 were imaged per animal in which 100 to 300 myelinated axon profiles with 4 or more myelin wraps were counted. For the assessment of the number of wraps for *shiverer* -/- and control all myelinated optic nerves were analyzed. For morphological analysis on longitudinal sections at least 20 myelinated axonal segments of 10-30 μm were assessed per animal.

Preparation of optic nerves for immunoelectron microscopy and immunolabeling of Tokuyasu sections of 50 nm were performed as described previously (Werner et al., 2007). In brief, optic nerves were freshly removed and immersion-fixed in 4% formaladehyde, 0.25 % glutaraldehyde (EM grade, Science Services, Munich, Germany) in phosphate buffer pH 7.3 as described in (Mobius et al., 2010). After a few hours of fixation, the nerves were embedded in 10% gelatin (Twee Torens, Delft, The Netherlands), infiltrated in 2.3 M sucrose over-night, mounted onto aluminum pins and frozen in lN$_2$. Tokuyasusections were prepared with a UC6 cryo-ultramicrotome (Leica, Vienna, Austria) and a cryoimmuno diamond knife (Diatome, Biel, Switzerland). For spinal cord samples mice at the age of 4 and 60 days were perfused transcardially with the same fixative described above. Then the spinal cord was carefully dissected and post-fixed for 12 hours in 4 % paraformaldehyde. The thoracic spinal cord portion was extracted from the bones and further processed for immuno electron microscopy. 400 nm Tokuyasu sections of the ventral column were collected on a super frost microscopic slice and processed for immunofluorescence staining.

Immunolabeling of ultrathin (50nm) Tokuyasu sections was performed as described in (Peters and Pierson, 2008) using antibodies directed against (VSV-G, MBP and CNP). Rabbit polyclonal antibodies were detected using protein A gold (10 nm, CMC Utrecht, the Netherlands). Monoclonal antibodies were also detected with protein A gold after incubation with a bridging antibody raised in rabbit. The quantification of the VSV-G labeling was performed in the corpus callosum on 100 axons wrapped by infected myelin sheath in 3 littermate animals for the 2 following conditions: 3 and 6 hours after VSV injection.

Serial block face imaging and 3D modeling software

Serial block face imaging data were obtained on a Helios Nanolab 650 dual beam scanning electron microscope equipped with a focused ion beam and images were obtained with a 2.0 kV electron beam using the back scatter electron (BSE) mode (immersion lens). The block

faces were imaged using the slice and view software with a dwell time of 3 μs. Total volumes of 16 x 13.8 x 40-55 μm^3 were recorded with a x/y pixel size of 4-6 nm during 4-7 days of acquisition in each sample. The alignment, the segmentation and the 3D reconstruction was performed using the Amira and the IMOD software (Kremer et al., 1996). Models derived from the experimental data were drawn in the Corel Draw 5 software suite.

VSV injections

For intracerbral (i.c.) infection, mice were anesthetized using isoflurane inhalation anesthesia.I.c. inoculation (10μl) was performed using a 28G insulin syringe over a period of 3 minutes. Solution contains VSV in balanced salt solution and 0.3% of monostral blue. The latter was added for better visualization of the injection side for histological processing. Following i.c. injection animals were euthanized either 3 or 6 hours later by intraperitoneal injection of pentobarbital and transcardially perfused with 4% PFA. Subsequently brains were dissected and small pieces of cortex with corpus callosum were postfixed with PFA for 4 hours and further processed for immunoelectron microscopy

Supplementary Material

Refer to Web version on PubMed Central for supplementary material.

Acknowledgements

References

Aggarwal S, Snaidero N, Pahler G, Frey S, Sanchez P, Zweckstetter M, Janshoff A, Schneider A, Weil MT, Schaap IA, et al. Myelin membrane assembly is driven by a phase transition of myelin basic proteins into a cohesive protein meshwork. PLoS Biol. 2013; 11:e1001577. [PubMed: 23762018]

Ainger K, Avossa D, Morgan F, Hill SJ, Barry C, Barbarese E, Carson JH. Transport and localization of exogenous myelin basic protein mRNA microinjected into oligodendrocytes. J Cell Biol. 1993; 123:431–441. [PubMed: 7691830]

Barres BA, Raff MC. Proliferation of oligodendrocyte precursor cells depends on electrical activity in axons. Nature. 1993; 361:258–260. [PubMed: 8093806]

Ben Geren B. The formation from the Schwann cell surface of myelin in the peripheral nerves of chick embryos. Exp Cell Res. 1954; 7:558–562. [PubMed: 13220597]

Blakemore WF. Schmidt-Lantermann incisures in the central nervous system. J Ultrastruct Res. 1969; 29:496–498. [PubMed: 5365373]

Bunge MB, Bunge RP, Ris H. Ultrastructural study of remyelination in an experimental lesion in adult cat spinal cord. J Biophys Biochem Cytol. 1961; 10:67–94. [PubMed: 13688845]

Bunge RP. Glial cells and the central myelin sheath. Physiol Rev. 1968; 48:197–251. [PubMed: 4866614]

Bunge RP, Bunge MB, Bates M. Movements of the Schwann cell nucleus implicate progression of the inner (axon-related) Schwann cell process during myelination. J Cell Biol. 1989; 109:273–284. [PubMed: 2745552]

Colman DR, Kreibich G, Frey AB, Sabatini DD. Synthesis and incorporation of myelin polypeptides into CNS myelin. J Cell Biol. 1982; 95:598–608. [PubMed: 6183276]

Czopka T, Ffrench-Constant C, Lyons DA. Individual oligodendrocytes have only a few hours in which to generate new myelin sheaths in vivo. Dev Cell. 2013; 25:599–609. [PubMed: 23806617]

Demerens C, Stankoff B, Logak M, Anglade P, Allinquant B, Couraud F, Zalc B, Lubetzki C. Induction of myelination in the central nervous system by electrical activity. Proc Natl Acad Sci U S A. 1996; 93:9887–9892. [PubMed: 8790426]

Farquhar MG. Progress in unraveling pathways of Golgi traffic. Annu Rev Cell Biol. 1985; 1:447–488. [PubMed: 3916320]

Fields RD, Stevens-Graham B. New insights into neuron-glia communication. Science. 2002; 298:556–562. [PubMed: 12386325]

Flores AI, Narayanan SP, Morse EN, Shick HE, Yin X, Kidd G, Avila RL, Kirschner DA, Macklin WB. Constitutively active Akt induces enhanced myelination in the CNS. J Neurosci. 2008; 28:7174–7183. [PubMed: 18614687]

Funfschilling U, Supplie LM, Mahad D, Boretius S, Saab AS, Edgar J, Brinkmann BG, Kassmann CM, Tzvetanova ID, Mobius W, et al. Glycolytic oligodendrocytes maintain myelin and long-term axonal integrity. Nature. 2012; 485:517–521. [PubMed: 22622581]

Goebbels S, Oltrogge JH, Kemper R, Heilmann I, Bormuth I, Wolfer S, Wichert SP, Mobius W, Liu X, Lappe-Siefke C, et al. Elevated phosphatidylinositol 3,4,5-trisphosphate in glia triggers cell-autonomous membrane wrapping and myelination. J Neurosci. 2010; 30:8953–8964. [PubMed: 20592216]

Gravel M, Peterson J, Yong VW, Kottis V, Trapp B, Braun PE. Overexpression of 2',3'-cyclic nucleotide 3'-phosphodiesterase in transgenic mice alters oligodendrocyte development and produces aberrant myelination. Mol Cell Neurosci. 1996; 7:453–466. [PubMed: 8875429]

Hildebrand C, Remahl S, Persson H, Bjartmar C. Myelinated nerve fibres in the CNS. Prog Neurobiol. 1993; 40:319–384. [PubMed: 8441812]

Ioannidou K, Anderson KI, Strachan D, Edgar JM, Barnett SC. Time-lapse imaging of the dynamics of CNS glial-axonal interactions in vitro and ex vivo. PLoS One. 2012; 7:e30775. [PubMed: 22303455]

Jessen KR, Mirsky R. The origin and development of glial cells in peripheral nerves. Nat Rev Neurosci. 2005; 6:671–682. [PubMed: 16136171]

Kirby BB, Takada N, Latimer AJ, Shin J, Carney TJ, Kelsh RN, Appel B. In vivo time-lapse imaging shows dynamic oligodendrocyte progenitor behavior during zebrafish development. Nat Neurosci. 2006; 9:1506–1511. [PubMed: 17099706]

Knobler RL, Stempak JG, Laurencin M. Nonuniformity of the oligodendroglial ensheathment of axons during myelination in the developing rat central nervous system. A serial section electron microscopical study. J Ultrastruct Res. 1976; 55:417–432. [PubMed: 933262]

Kremer JR, Mastronarde DN, McIntosh JR. Computer visualization of three-dimensional image data using IMOD. J Struct Biol. 1996; 116:71–76. [PubMed: 8742726]

Lappe-Siefke C, Goebbels S, Gravel M, Nicksch E, Lee J, Braun PE, Griffiths IR, Nave KA. Disruption of Cnp1 uncouples oligodendroglial functions in axonal support and myelination. Nat Genet. 2003; 33:366–374. [PubMed: 12590258]

Laursen LS, Chan CW, Ffrench-Constant C. Translation of myelin basic protein mRNA in oligodendrocytes is regulated by integrin activation and hnRNP-K. J Cell Biol. 2011; 192:797–811. [PubMed: 21357748]

Lee Y, Morrison BM, Li Y, Lengacher S, Farah MH, Hoffman PN, Liu Y, Tsingalia A, Jin L, Zhang PW, et al. Oligodendroglia metabolically support axons and contribute to neurodegeneration. Nature. 2012; 487:443–448. [PubMed: 22801498]

Liu J, Dietz K, Deloyht JM, Pedre X, Kelkar D, Kaur J, Vialou V, Lobo MK, Dietz DM, Nestler EJ, et al. Impaired adult myelination in the prefrontal cortex of socially isolated mice. Nat Neurosci. 2012; 15:1621–1623. [PubMed: 23143512]

Makinodan M, Rosen KM, Ito S, Corfas G. A critical period for social experience-dependent oligodendrocyte maturation and myelination. Science. 2012; 337:1357–1360. [PubMed: 22984073]

Pedraza L, Huang JK, Colman D. Disposition of axonal caspr with respect to glial cell membranes: Implications for the process of myelination. J Neurosci Res. 2009; 87:3480–3491. [PubMed: 19170162]

Mobius W, Cooper B, Kaufmann WA, Imig C, Ruhwedel T, Snaidero N, Saab AS, Varoqueaux F. Electron microscopy of the mouse central nervous system. Methods Cell Biol. 2010; 96:475–512. [PubMed: 20869535]

Peters PJ, Pierson J. Immunogold labeling of thawed cryosections. Methods Cell Biol. 2008; 88:131–149. [PubMed: 18617032]

Pereira JA, Lebrun-Julien F, Suter U. Molecular mechanisms regulating myelination in the peripheral nervous system. Trends Neurosci. 2012; 35:123–134. [PubMed: 22192173]

Ridley AJ. Life at the leading edge. Cell. 2011; 145:1012–1022. [PubMed: 21703446]

Salzer JL, Brophy PJ, Peles E. Molecular domains of myelinated axons in the peripheral nervous system. Glia. 2008; 56:1532–1540. [PubMed: 18803321]

Sherman DL, Brophy PJ. Mechanisms of axon ensheathment and myelin growth. Nat Rev Neurosci. 2005; 6:683–690. [PubMed: 16136172]

Sobottka B, Ziegler U, Kaech A, Becher B, Goebels N. CNS live imaging reveals a new mechanism of myelination: The liquid croissant model. Glia. 2011; 59:1841–1849. [PubMed: 21887712]

Toyama BH, Savas JN, Park SK, Harris MS, Ingolia NT, Yates JR 3rd, Hetzer MW. Identification of long-lived proteins reveals exceptional stability of essential cellular structures. Cell. 2013; 154:971–982. [PubMed: 23993091]

Trapp BD, Andrews SB, Wong A, O'Connell M, Griffin JW. Co-localization of the myelin-associated glycoprotein and the microfilament components, F-actin and spectrin, in Schwann cells of myelinated nerve fibres. J Neurocytol. 1989; 18:47–60. [PubMed: 2468742]

Trapp BD, Moench T, Pulley M, Barbosa E, Tennekoon G, Griffin J. Spatial segregation of mRNA encoding myelin-specific proteins. Proc Natl Acad Sci U S A. 1987; 84:7773–7777. [PubMed: 3478726]

Tyler WA, Gangoli N, Gokina P, Kim HA, Covey M, Levison SW, Wood TL. Activation of the mammalian target of rapamycin (mTOR) is essential for oligodendrocyte differentiation. J Neurosci. 2009; 29:6367–6378. [PubMed: 19439614]

Velumian AA, Samoilova M, Fehlings MG. Visualization of cytoplasmic diffusion within living myelin sheaths of CNS white matter axons using microinjection of the fluorescent dye Lucifer Yellow. Neuroimage. 2011; 56:27–34. [PubMed: 21073961]

Wake H, Lee PR, Fields RD. Control of local protein synthesis and initial events in myelination by action potentials. Science. 2011; 333:1647–1651. [PubMed: 21817014]

Webster HD. The geometry of peripheral myelin sheaths during their formation and growth in rat sciatic nerves. J Cell Biol. 1971; 48:348–367. [PubMed: 4928020]

Werner HB, Kuhlmann K, Shen S, Uecker M, Schardt A, Dimova K, Orfaniotou F, Dhaunchak A, Brinkmann BG, Mobius W, et al. Proteolipid protein is required for transport of sirtuin 2 into CNS myelin. J Neurosci. 2007; 27:7717–7730. [PubMed: 17634366]

Young KM, Psachoulia K, Tripathi RB, Dunn SJ, Cossell L, Attwell D, Tohyama K, Richardson WD. Oligodendrocyte Dynamics in the Healthy Adult CNS: Evidence for Myelin Remodeling. Neuron. 2013; 77:873–885. [PubMed: 23473318]

Zhao M, Song B, Pu J, Wada T, Reid B, Tai G, Wang F, Guo A, Walczysko P, Gu Y, et al. Electrical signals control wound healing through phosphatidylinositol-3-OH kinase-gamma and PTEN. Nature. 2006; 442:457–460. [PubMed: 16871217]
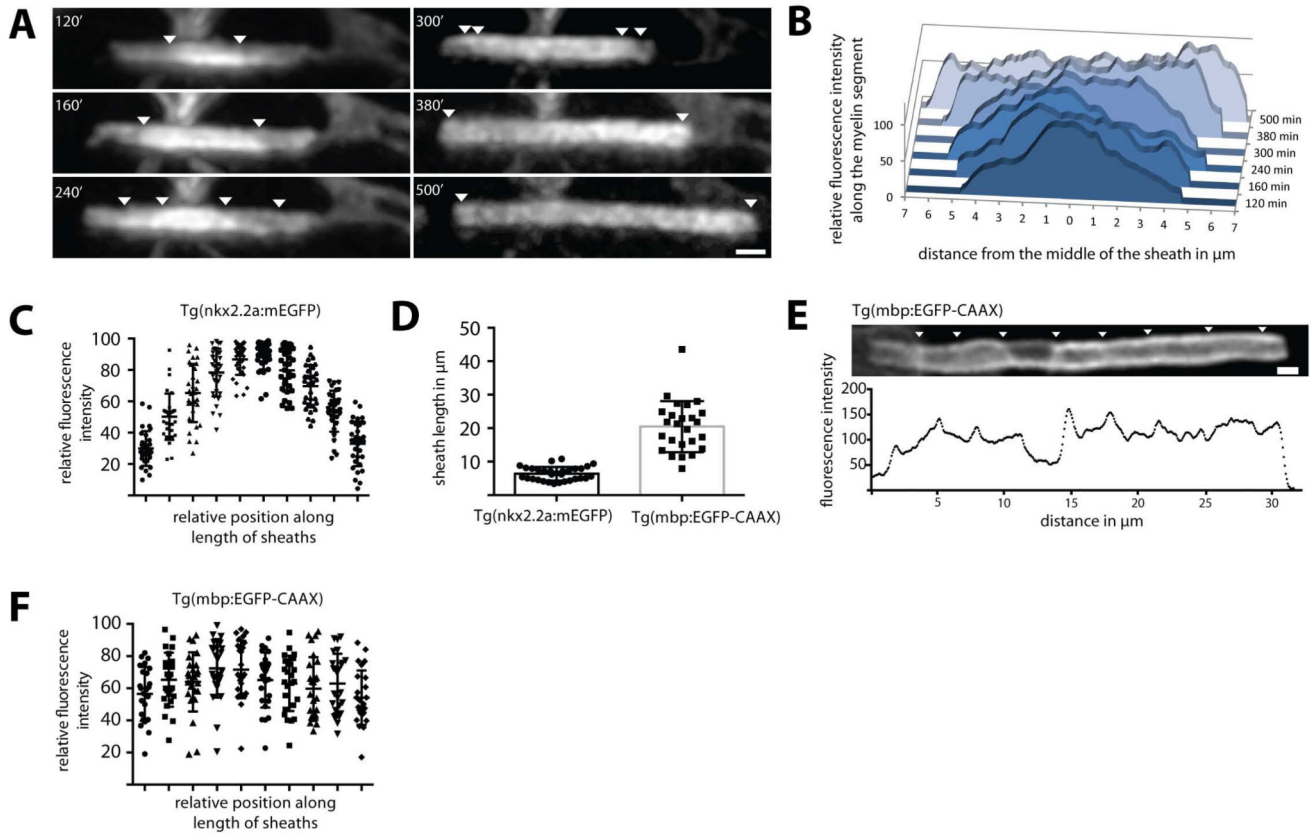
Figure 1. Live imaging of myelin formation in zebrafish.
(A) Visualization of the growth of a myelin segment in live Tg(nkx2.2a:meGFP) zebrafish for 500 minutes at 3 days postfertilization (dpf). The steps in fluorescence intensity are pointed with arrowheads. (B) Graphic representation of the relative fluorescence along the myelin segment over time shown in (A). (C) Graph showing relative fluorescence intensity measurements for 32 nkx2.2a:mEGFP expressing nascent myelin sheaths along their length. This indicates higher average intensity at the centre of sheaths relative to their ends. Bars show mean ± SD (D) Graph showing length of 32 myelin sheaths imaged using the nkx2.2a:mEGFP compared to 25 segments visualized in the mbp:EGFP-CAAX zebrafish line. (E) Lateral view of a mbp:EGFP-CAAX expressing mature myelin sheath at 4 dpf shows fluorescence intensity pattern along the maturing myelin segment. Arrowheads point to areas of higher fluorescence intensity. (F) Graph showing relative fluorescence intensity measurements for 25 mbp:EGFP-CAAX expressing mature myelin sheaths along their length. Scale bars= 1μm. See also Figure S1 and Movie S1.
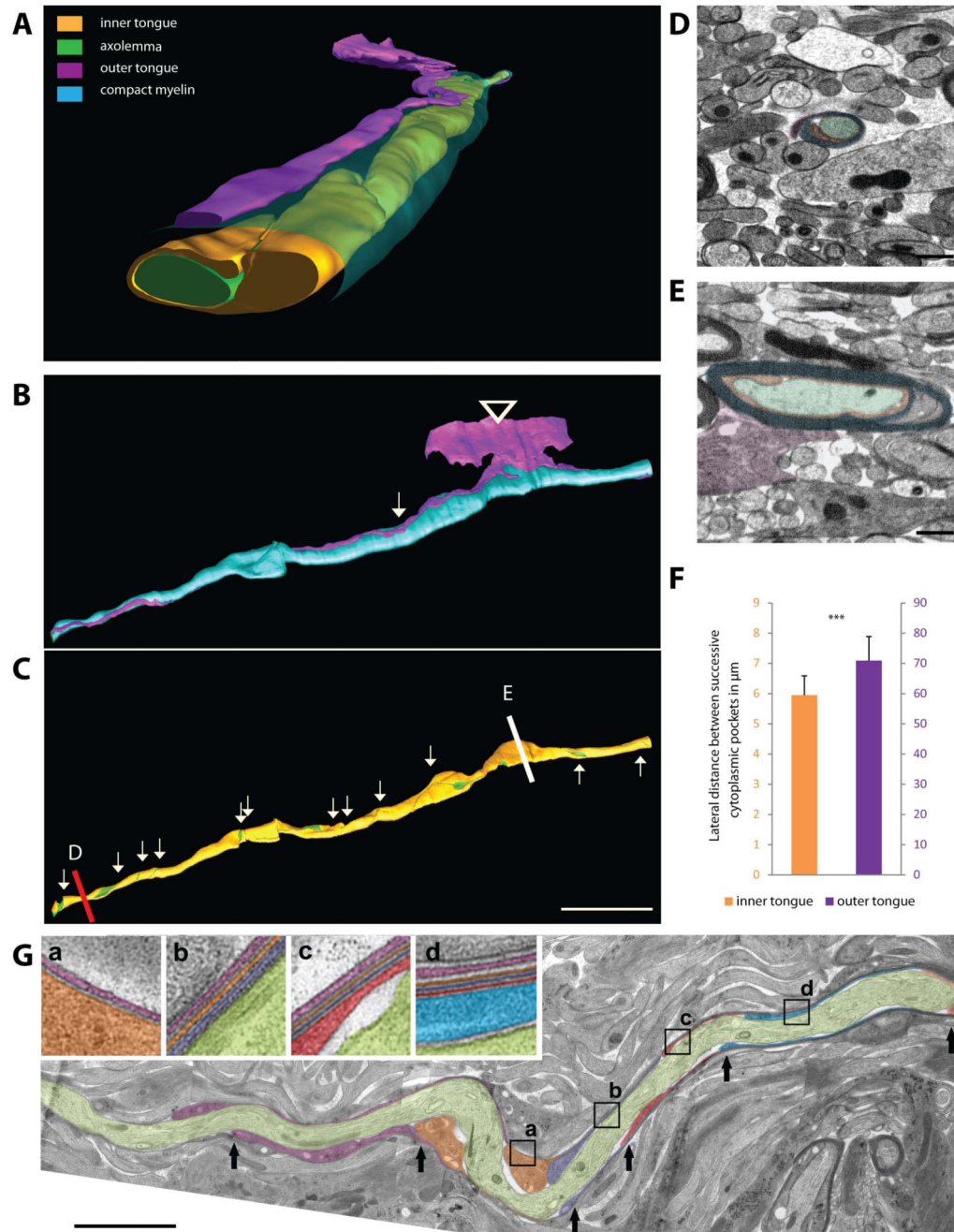
Figure 2. Three-dimensional reconstruction of myelin structure in high-pressure frozen optic nerves.

(A,B,C) High-resolution 3D reconstruction of a forming myelin segment showing the structure of the inner and outer layers (green: axolemma, orange: inner tongue, cyan: compacted myelin, purple: outer tongue). (B) The outer tongue is connected to the oligodendrocyte cell body (arrowhead) and the position where the outer tongue has made one turn is marked by an arrow. (C) The inner tongue coils around the axon from a 2 wraps thick myelin sheath (red line; cross-section shown in D) up to 11 wraps (white line; cross-section shown in E). Every turn is indicated by an arrows pointing down; and by arrows

pointing up where the inner tongue is unwinding towards the other end of the sheath. Scale bar= 10μm.(D) Cross-sectional image of the area indicated with a red line (myelin with 2 wraps). (E) Cross-sectional image of the area indicated with a white line (myelin with 11 wraps). (F) Average distance between 2 lateral cytoplasmic-rich edges of successive myelin layers of the inner and outer tongue. Bars show mean ± SD (n=3 animals with 45 different axons). (G) Representative myelin sheath of P10 mouse optic nerve obtained by serial sectioning of high-pressure frozen tissue and imaged by TEM. An arrow is pointing to the lateral edge of successive myelin layers; each in a different color. (a-d) In the enlarged areas the individual myelin layers are marked by different colors and followed along the segment; the position of the zoomed areas is shown as a box. Scale bar= 5μm. See also Figure S2 and Movie S2,3,4.
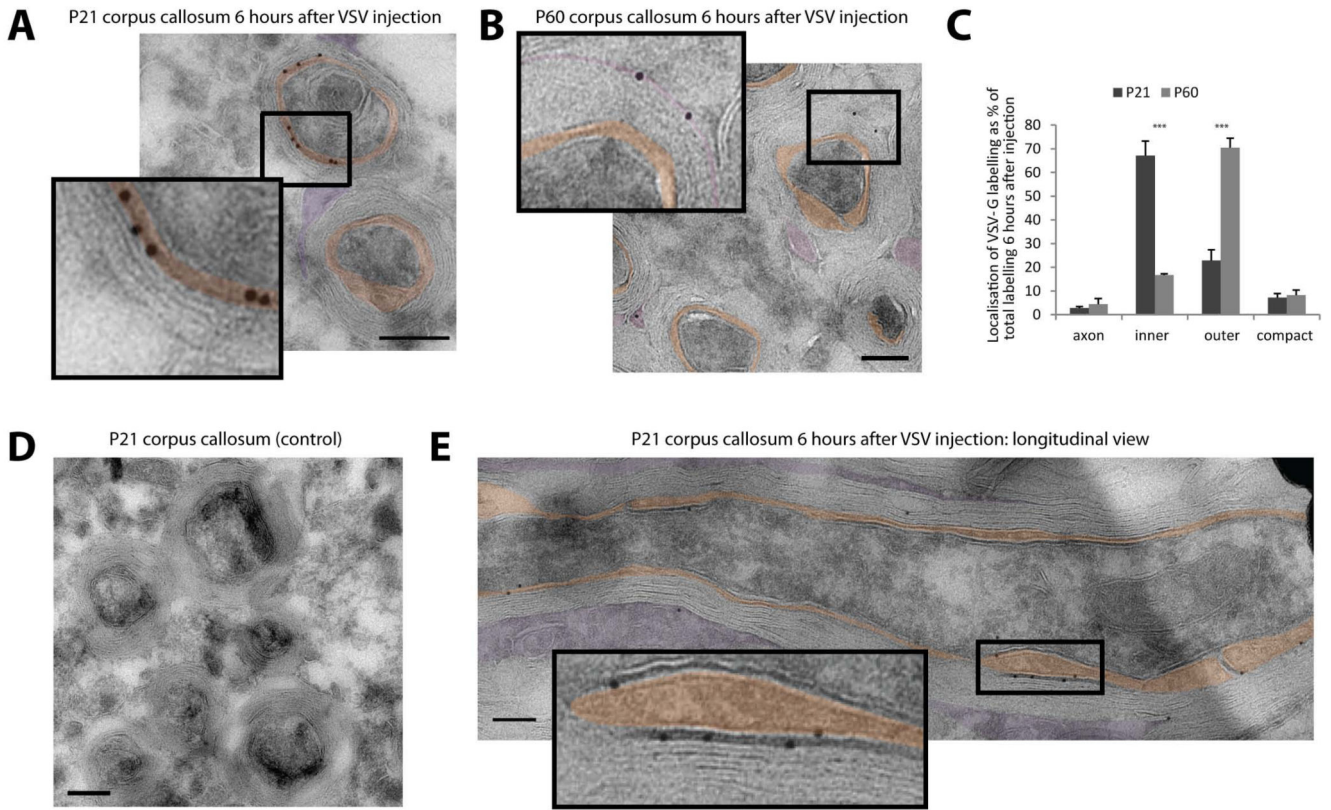
Figure 3. Tracking membrane trafficking using the vesicular stomatitis virus G protein *in vivo*.
(A-B) High-titer stocks of VSV were injected into the corpus callosum of P21 and P60 mice. The subcellular localization of VSV-G in the myelin sheath was determined by immunoelectron microscopy 6 hours after infection at P21 (A) and P60 (B) mice (orange: inner tongue, purple: outer tongue). (C) Quantification of the VSV-G labeling distribution within the different domains of the myelin sheath at P21 and P60. Bars show mean ± SD (n=3, 100 axon per animal, ***p < 0.001, t-test). (D) No background staining of the VSV-G antibody after control injections without virus into the corpus callosum at P21. (E) Localization of VSV-G at the inner layers in longitudinal section of P21 corpus callosum 6 hours after VSV injection. Scale bars= 200nm; gold size= 10 nm. See also Figure S3.
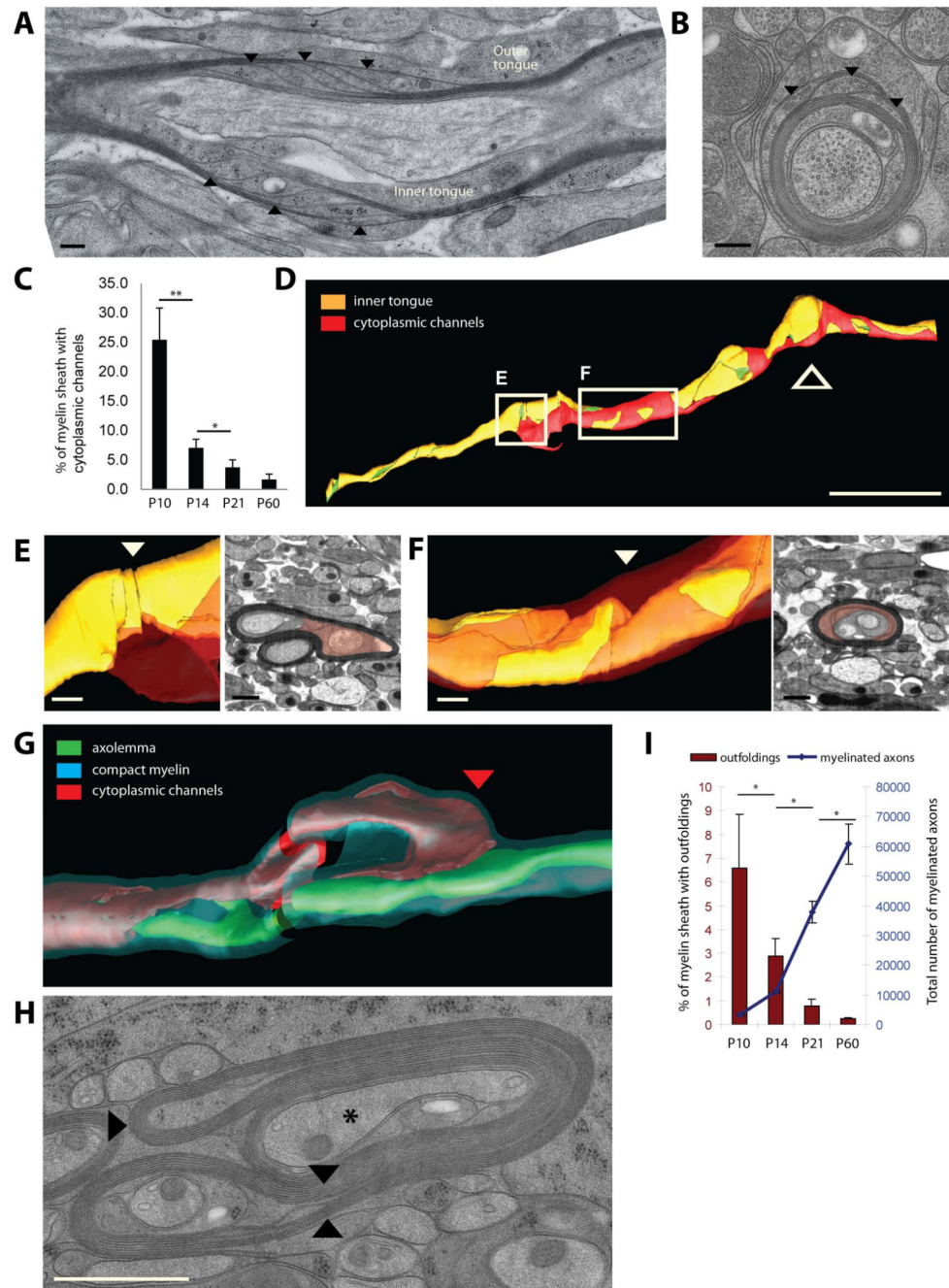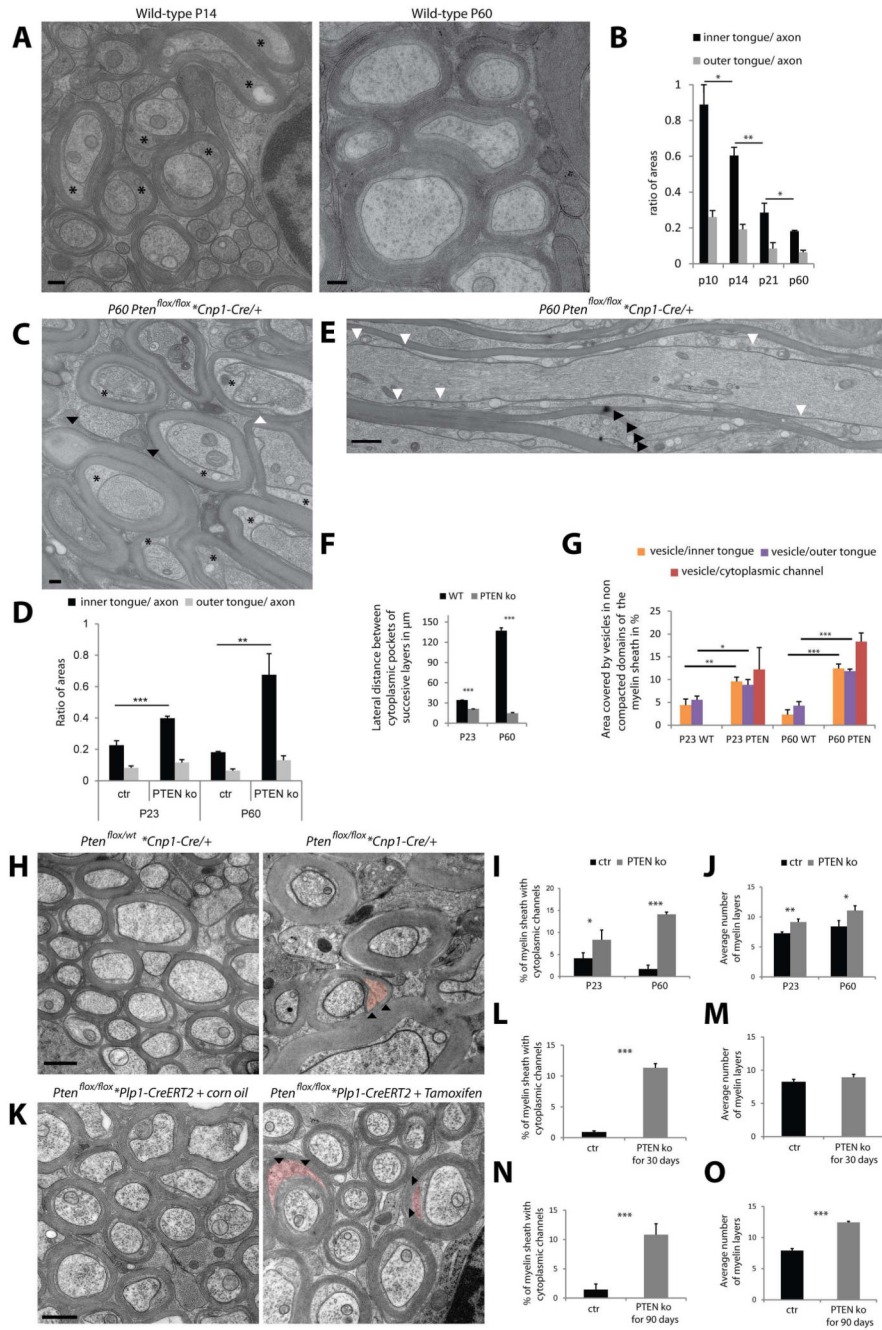
Figure 4. Cytoplasmic channels and myelin outfoldings appear transiently in developing myelin sheaths.

(A, B) Longitudinal and cross sections of P10 optic nerve myelinated axons showing cytoplasmic channels within the compact myelin indicated by arrow heads. Scale bar=200nm. (C) Percent of myelin sheaths with cytoplasmic channels at P10, P14, P21 and P60. Bars show mean ± SD (n=3, 200 axons per animal, *p < 0.05 **p < 0.01, t-test). (D) Three dimensional organisation of the cytoplasmic channels (red: cytopalsmic channels, orange: inner tongue, green: axolemma) along the myelin sheath (thick arrow signals the location the oligodendrocyte process). Scale bar= 10μm. (E,F) Model and electron

microscopy views of the area where the cytoplasmic channels (red) reach the inner tongue (arrowhead: position of the EM views). Scale bar= 500nm. (G) Spatial organization of cytoplasmic channels (red) running inside the outfolding and reaching the inner tongue at the lateral end of the outfolding (red arrow head). (H) Cross section morphology of myelin outfolding (arrowheads) in P10 high pressure frozen optic nerve (star labels the axon with a normal myelin sheath). (I) Amount of myelin outfoldings in myelinated fibers in optic nerves between P10 and P60. Bars show mean ± SD (n=3, 200-800 axons per animal, *p < 0.05, t-test). See also Figure S4.

Figure 5. Regulation of cytoplasmic channels, inner tongue size and myelin sheath growth by PI(3,4,5)P3 levels.

(A) Electron micrograph of high pressure frozen wild-type optic nerve showing larger inner tongue at P14 (stars) as compared to P60. Scale bar= 200nm. (B) Relative size of the inner and outer tongue area to the axonal area between P10 and P60. (C) Electron micrograph of P60 conditional *Pten* deficient mice (*Pten* KO; *Pten*^flox/flox *Cnp1- Cre/+*) optic nerve showing enlarged inner tongues (stars). (D) Relative size of the inner and outer tongue area to the axonal area at P23 and P60 for the *Pten* mutant (wild type P60 data from panel B for comparison). (E) Longitudinal view of P60 *Pten* mutant optic nerve show the short lateral

distances between successive inner layers (white arrow heads) and the large cytoplasmic channels within the compact myelin (black arrow heads). (F) Average distance between 2 lateral cytoplasmic-rich edges of successive myelin layers at P23 and P60 for the *Pten* mutant compared to wild-type. (G) Quantification of the area covered by vesicular structures in *Pten* deficient animals as compared to wild-type at P23 and P60 (data used for wild-type are from S4). (H) Electron micrograph of myelin from conditional *Pten* deficient mice (*Pten* KO; *Pten*$^{flox/flox}$ **Cnp1-Cre/+*) optic nerve compared to the control (Control; *Pten*$^{flox/wt}$ **Cnp1-Cre/+*) at P60 (arrowheads pointing at colored cytoplasmic channels). (I,J) Amount of myelin sheaths with cytoplasmic channels in cross-sections and measurement of the myelin thickness in control and *Pten* mutant optic nerves. (K) Electron micrograph of optic nerve myelin after tamoxifen-induced conditional inactivation for 4 weeks of *Pten*$^{flox/flox}$**Plp1-CreERT2* mice in the adult (P60) compared to the control (arrowhead pointing at colored cytoplasmic channels). Scale bar= 500nm. (L-O) Amount of myelin sheaths with cytoplasmic channels in cross-sections and measurement of the myelin thickness in control and after tamoxifen-induced conditional inactivation of *Pten* for 4 weeks (L,M) and for 12 weeks (N,O). Bars shown in all graphs mean ± SD (n=3, 100-200 axons per animal, 20 axons per animals for F; *p < 0.05, **p < 0.01, ***p < 0.001, t-test). See also Figure S5.
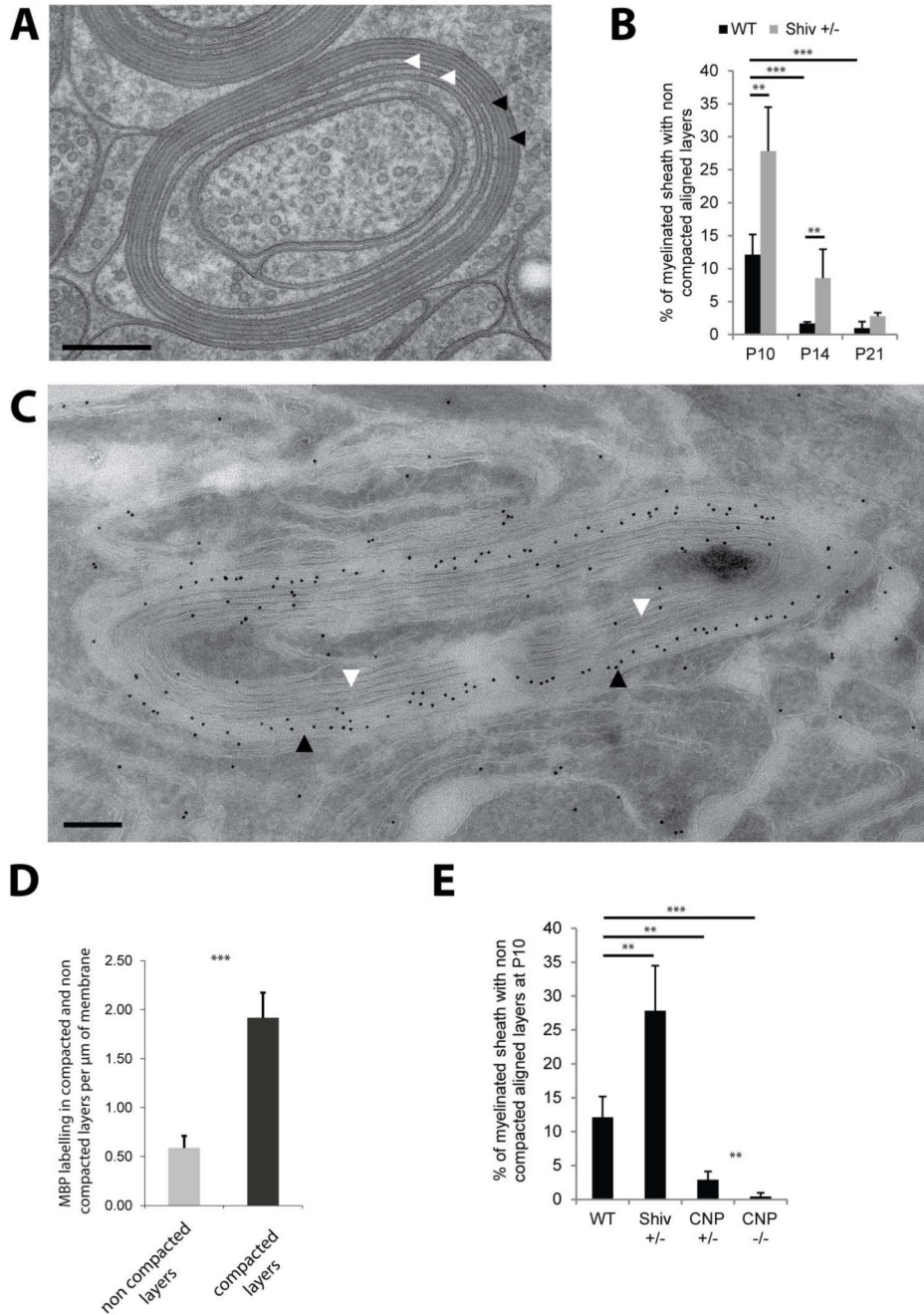
Figure 6. Myelin compaction from the outer to the inner layers is regulated by MBP and CNP levels.

(A) Cross section of P10 wild-type myelin sheath with outer layers compacted (black arrows) and inner layers non-compacted (white arrows). (B) Amount of myelinated axons with non-compacted layers in wild-type and *shiverer* heterozygote (Shiv +/-) optic nerves between P10 and P21. (C) Immunoelectron micrograph for MBP of a partially compacted myelin sheath of P10 wild-type optic nerve (black arrows pointing at compacted layers and white arrows to the non-compacted layers). Scale bars= 200nm. Gold size= 10nm. (D) Quantification of MBP labeling per μm of membrane in the compacted and non-compacted

layers of P10 wild-type myelin sheaths. (E) Amount of myelinated axons with non-compacted layers in wild-type, Shiv +/-, CNP +/- and CNP -/- at P10. Bars show mean ± SD (n=3-5, 120-200 axons per animal, **p < 0.01, ***p < 0.001, t-test). See also Figure S6.
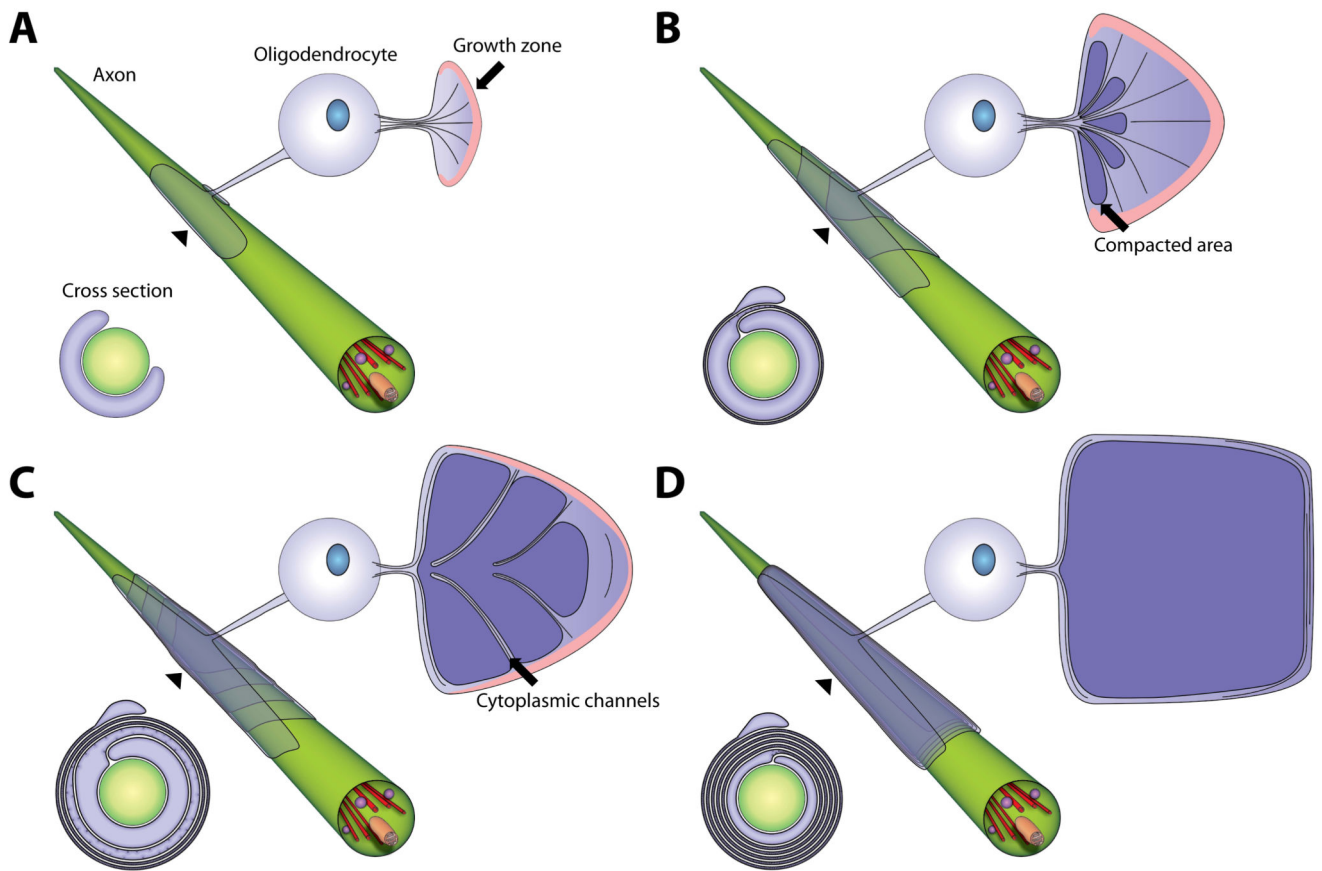
Figure 7. Model of myelin biogenesis in the CNS.
(A-D) Model of a developing myelin sheath in a wrapped, unwrapped and cross section view. The unwrapped representation shows the geometry and the development of the sheath and the localization of the cytoplasmic channels, which connect the cell body and the growth zone at the inner tongue. The growth zone is colored in pink and compacted myelin in dark violet. The wrapped representation shows the position of the layers when wrapped around the axon. The cross sections show the state of compaction during myelin growth. See also Figure S7 and Movie S5.